Accepted submission to the ASME 2025 Pressure Vessels & Piping Conference

SIMULATION OF ELECTROMAGNETIC LITHIUM CYLINDER COMPRESSION FOR APPLICATIONS IN MAGNETIZED TARGET FUSION

Nick Sirmas[1,*], Jean-Sebastien Dick[1], Scott Bernard[1], Yu Miao[1], Lemuel Santos[1], Jake Hobbis[1], Claire Preston[1], Anthony Lee[1], Sean Cameron[1], Piotr Forysinski[1]

[1]General Fusion, Richmond, British Columbia, Canada

ABSTRACT

General Fusion is developing Magnetized Target Fusion (MTF) as a practical means of producing deuterium-tritium fusion power. Lawson Machine 26 (LM26) is an MTF demonstration that integrates General Fusion's operational Plasma Injector 3 (PI3) with a solid lithium cylindrical shell compression system. The lithium plasma liner is electromagnetically compressed by a stack of coils via a "theta-pinch".

Prototype Zero (P0), a testbed at 1:4 scale of LM26, was designed and commissioned to de-risk the complex compression process and validate modeling tools in the absence of plasma to ensure accurate predictions for LM26 operations. Prototype Zero comprises 48 coil turns that are arranged to compress a lithium cylinder with an axial height up to 280 mm, outer radius of 218 mm, and thickness ranging from 10 to 20 mm. Capacitors supply up to 1 MJ of energy to the coils, resulting in the cylinders being compressed in 0.7 to 1 ms at radial velocities exceeding 300 m/s. The center shaft of the machine is composed of two cones which form an hourglass shape and serve to further compress the cylinder in the axial direction.

A 2D axisymmetric numerical model was developed using ANSYS LS-DYNA to predict the trajectory of the liner. A circuit model was implemented to represent the RLC circuit connected to the driving coils. LS-DYNA predictions of the liner position were compared to experimental measurements obtained using diagnostic equipment mounted within the center shaft cones. Diagnostics included photon Doppler velocimetry (PDV) to measure radial velocity at the mid-plane of the lithium cylinder, and structured light reconstruction (SLR) to track the axial profile of the cylinder during compression. An alternate arrangement employed a single center shaft cone, enabling direct visualization of the compression with a high-speed camera through a window.

Simulations were conducted for a selection of Prototype Zero compression shots and compared with experimental measurements. Results confirm the accuracy of the modelling technique in predicting the shape of a cylindrical lithium liner undergoing electromagnetic compression. This study provides critical validation of the modeling tools that supported the design and build of General Fusion's large-scale LM26 fusion demonstration machine, which began operating in early 2025.

*Corresponding author: nick.sirmas@generalfusion.com

Keywords: Electromagnetic Compression, Lithium, Fusion, ANSYS LS-DYNA, Magnetized Target Fusion (MTF), Photon Doppler Velocimetry

1. INTRODUCTION

The Magnetized Target Fusion (MTF) technology being developed by General Fusion utilizes mechanical compression of a deuterium-tritium (DT) plasma target formed through coaxial helicity injection (CHI). This compression is achieved using a rotating liquid metal flux conserver (liner) [1]. A key advantage of this approach lies in its liquid metal first wall, which serves as a breeding blanket for tritium, a neutron shield, and a heat carrier. However, the primary challenge in this approach is achieving sufficiently rapid and symmetric plasma compression to ensure that heat losses to the surroundings—through radiation, contamination, and turbulence—remain significantly lower than the plasma heating rate [2–4].

General Fusion's Plasma Compression Science (PCS) experimental campaign assessed this technology by employing chemically driven implosions of spherical, 38 cm internal diameter aluminum flux conservers [5]. The campaign's most promising results were obtained during the PCS-16 compression which used a spherical tokamak plasma configuration. A significant increase in neutron generation was achieved demonstrating successful plasma compression with a compression time on the order of 160 μs. These findings led to the development of new methodologies for predicting MHD resistive instabilities [6, 7]. Further work was also carried out to study piston-driven liquid liner compression [8].

In 2017, General Fusion introduced a new generation plasma injector, PI3 [9]. This injector has demonstrated the ability to produce plasma with electron and ion temperatures exceeding 400 eV, densities up to 4e19 m^{-3}, and thermal confinement times of 10 ms [10, 11]. These pre-compression plasma performance parameters are significantly superior to those achieved by the plasma injectors used in the PCS campaign.

From 2023 to 2024, General Fusion designed and assembled the Lawson Machine 26 (LM26) to demonstrate its MTF technology at large scale. The machine began operating in early 2025 and has successfully compressed a large-scale magnetized plasma with lithium. LM26 integrates the PI3 plasma injector with a spherical tokamak cavity and an electromagnetic compres-

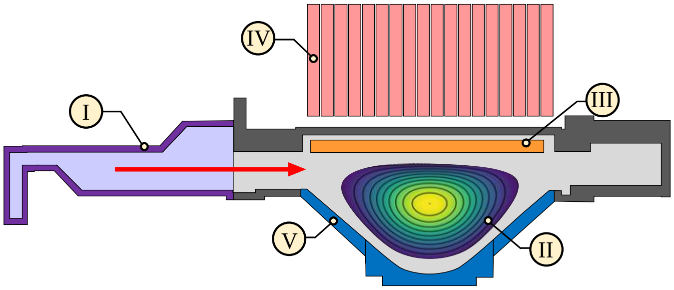

FIGURE 1: Partial cross-section of the LM26 machine showing the plasma injector connected to the electromagnetic compressor. I) Plasma injector, injection direction shown. II) Plasma. III) Lithium liner. IV) Compression coils. V) Center shaft with diagnostic equipment.

sor, also known as a theta-pinch apparatus. The LM26 machine features a solid lithium liner as the flux conserver, depicted in Fig. 1. The lithium liner has an internal radius of approximately 800 mm, axial length of 1000 mm and compresses plasmas in less than 5 ms. The compressor and fusion vessel designs were guided by simulations and small-scale prototypes.

Initially, a lithium ring compression testbed was built to evaluate the performance and symmetry of electromagnetic compression. The ring compressor could compress rings with a radius of approximately 250 mm in under one millisecond, using eight coil turns connected to a 245 kJ capacitor bank [12]. Eleven lithium rings were compressed during the experimental campaign. Instances of symmetry loss, which resulted in visible toroidal buckling, were utilized to validate a linear dynamic stability model for lithium rings [13]. The model successfully predicted the dominant unstable modes of the rings that buckled during compression.

A 2D axisymmetric modelling methodology using ANSYS LS-DYNA was developed to compare with ring trajectories from test [12]. The methodology utilized the electromagnetic solver in LS-DYNA, which combines the finite element method (FEM) solver for structural dynamics with the boundary element method (BEM) solver for electromagnetics [14]. Simulation required characterization of the plastic behaviour of lithium, which was obtained *via* hammer drop tests, with results fit to a Johnson-Cook material model [15]. The simulations aligned closely with experimental radial trajectories and magnetic flux density probe measurements. However, this methodology relied on measured coil currents as inputs, limiting its predictive capability for pulsed power system design (*e.g.*, capacitance, voltage), coil configurations (*e.g.*, spacing, number of turns) and compression performance.

Prototype Zero (P0) is the next testbed developed to de-risk the compression of solid lithium liners in LM26 and is the focus of this paper. Prototype Zero is built at 1:4 scale of LM26 and differs from the previously tested ring compressor by its taller lithium cylinders (250 mm in height *vs.* 54 mm). The machine includes a central conical structure similar to the LM26 spherical tokamak plasma cavity. Diagnostic equipment is mounted within the cones to measure the liner shape and position during compression.

This paper details enhancements to the simulation methodology, validated against results from Prototype Zero. A new circuit model has been incorporated into LS-DYNA, enabling a fully integrated approach for replicating experiment, from capacitor bank activation to peak compression of the lithium liner. The improved modelling methodology is validated across three shot configurations.

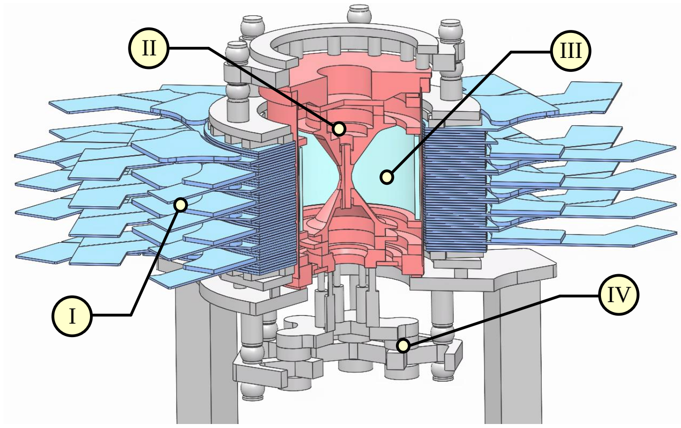

FIGURE 2: Overview of components of experimental apparatus. I) Compression coils. II) Test cartridge. III) Lithium liner. IV) Support structure.

The paper is divided into three sections. The first section presents the experimental apparatus and its diagnostics. The second section details the numerical methodology and the new circuit model. The last section presents the numerical results and how they compare to experiment.

2. EXPERIMENTAL APPARATUS

The experimental apparatus is comprised of a high voltage power supply, a set of theta-pinch coils, and a "cartridge": a replaceable assembly containing the lithium liner, a center shaft structure, and diagnostic equipment. The cartridge is installed into the center of the coil stack and is replaced after every liner compression (referred to as a shot). A simplified diagram of the compression coils and cartridge is shown in Fig. 2.

Figure 3 shows a simplified axisymmetric cross section of the key components of the compressor. The apparatus is composed of 48 coil turns that are arranged to compress a lithium cylinder with an axial height up to 280 mm, outer radius of 218 mm, and thickness ranging from 10 to 20 mm.

Two cartridge configurations exist for the apparatus. The first configuration, shown in Fig. 3a), includes a center shaft that is composed of two cones which form an hourglass shape and serve to further compress the cylinder in the axial direction. In the second configuration, shown in Fig. 3b), the top center shaft cone is removed and replaced with a straight shaft and window to allow direct visualization from the top of the cartridge.

2.1 Coils and Power Supply

The coil assembly is composed of 48 single-turn, flat, 6.4 mm thick aluminum plates with a nominal inner diameter of 468 mm, stacked to a total height of 370 mm. Adjacent plates are separated by a layer of laminated insulation (DMD). Three plates (turns) comprise a coil, for a total of sixteen coils in the assembly. A simplified representation of a single turn is shown in Fig. 4.

The layout of the compression coils is shown in Fig. 3a). The sixteen coils are connected to eight isolated circuits, with each

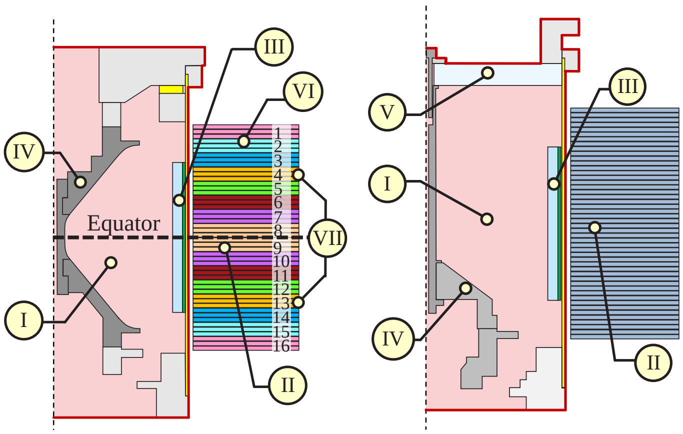

(a) Two-cone configuration **(b) Single-cone and window configuration**

FIGURE 3: Simplified axisymmetric representation of the components of the experimental apparatus for the two types of cartridges. I) Cartridge. II) Compression coils. III) Liner. IV) Center shaft / cones. V) Window / viewport. VI) Coil (3 plate stack). VII) Pair coil (same circuit).

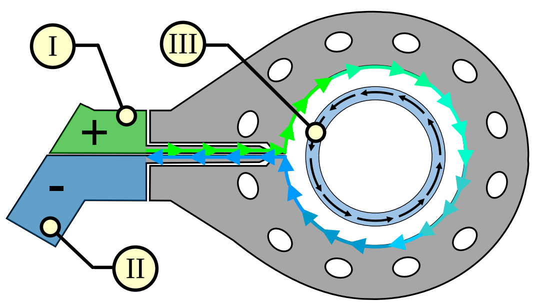

FIGURE 4: Simplified single-turn compression coil with current path shown. I) Positive electrode. II) Negative electrode. III) Lithium liner with induced current shown.

circuit composed of a pair of two coils connected in parallel. The parallel pair coils are symmetric about the mid-plane of the coil assembly, known as the equator.

Each isolated circuit is an RLC circuit with a diode, as depicted in Fig. 5. Estimated circuit parameters are shown in Table 1. Each circuit is connected to twelve high voltage 104 μF capacitors, which can operate at up to 16 kV. With all circuits active at maximum capacity, the apparatus can supply up to 1 MJ of energy to the coils. During operation, select circuits can be activated to study compression trajectories, while the remainder of the circuits are 'open-circuited', *i.e.* coils can be treated as having zero current in the azimuthal direction.

2.2 Lithium Cylinders

The lithium cylinders are produced in-house using custom casting and processing equipment. A casting is produced by pumping liquid lithium from a reservoir into a mold. The outer wall of the mold is a G7 fiberglass tube that remains with the casting for the rest of the experiment to provide structural support during handling. The inner diameter and two end faces of the casting are turned on a custom lathe to remove surface impurities and control the dimensions of the lithium cylinder. All casting, processing, and installation operations are performed under an argon atmosphere to prevent lithium reactions with air. A lithium cylinder after turning is shown in Fig. 6.

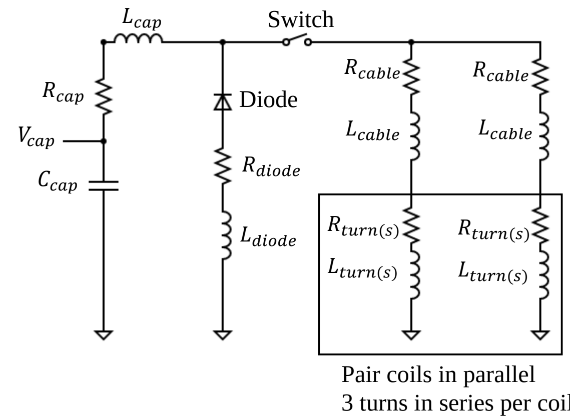

FIGURE 5: Schematic of simplified circuit that connects power supply to the coils in test apparatus.

TABLE 1: Circuit parameters

Parameter	Value
V_{cap}	Shot dependent
C_{cap}	1.248 mF
R_{cap}	6.457 mΩ
L_{cap}	232.3 nH
R_{diode}	1.70 mΩ
L_{diode}	65 nH
R_{cable}	12.85 mΩ
L_{cable}	910 nH
N_{turns}	3

FIGURE 6: Lithium cylinder after machining inside argon filled glovebox.

2.3 Diagnostics and Data Collection

Three diagnostic subsystems are used to record the shape of the compressing lithium liner: structured light reconstruction (SLR), photon Doppler velocimetry (PDV), and direct imaging. SLR is used in the double-cone configuration and direct imaging is used in the single-cone/window configuration. PDV is used in both configurations.

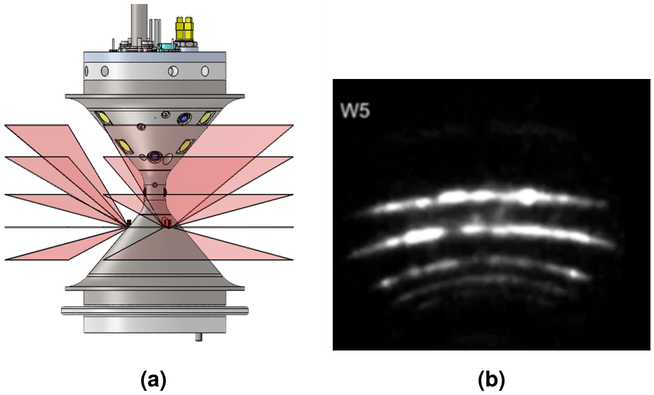

FIGURE 7: SLR diagnostic system in Prototype Zero: a) Model view of cones and SLR laser semi-arcs, b) frame from video of laser semi-arcs on lithium liner viewed through fisheye and imaging fiber.

2.3.1 Structured Light Reconstruction (SLR). The SLR subsystem consists of laser pattern projection and imaging apparatus. Briefly, a 15 W, 637 nm, 400 µm diameter multimode fiber-coupled laser source (CivilLaser) is collimated and passes through an access port in the upper cone. It then impinges on a custom diamond-turned reflective optic mounted in the lower cone that creates five semi-arcs of laser light aimed at different axial positions on the liner, which cover approximately 120 degrees of azimuthal range as shown in Fig. 7a). This projection apparatus is replicated twice more to provide near-complete azimuthal coverage. Images of the laser semi-arcs on a calibration grid at two different distances are taken to map their 3D shape as-installed.

Commercial fisheye lenses (ChanCCTV CH3631DB) are mounted on the upper cone surface in six different positions allowing visualization of the entire liner surface until the lenses are covered by the compressing lithium liner. Each lens image is coupled into a 13k pixel imaging plastic optical fiber (Asahi-Kasei MCL-2000-24), and these are subsequently relayed to a single high-speed camera (Photron Nova S12). Optical intrinsic (distortion) and extrinsic (rotation, position) parameters of the imaging assemblies are obtained by imaging calibration patterns.

The laser semi-arcs' diffuse reflections from the lithium liner can be viewed through the imaging assemblies as seen in Fig. 7b). As the lithium liner compresses, the semi-arcs are tracked by high-speed video capture. Reconstruction of the 3D shape of the inner surface of the liner during the implosion is carried out using an algorithm similar to that described previously [8]. The standard deviation of the scatter in the SLR measurements when compared to the initial liner geometry is found to be ±5 mm and used as the uncertainty for all SLR measurements. Sources of error include uncertainties in the optics hardware and mounting in the shaft and relative to the calibration equipment contributing to uncertainty in the optical calibration parameters. Additionally, the low fiber optical resolution limits the precision of the laser semi-arc position extraction from the images.

2.3.2 Photon Doppler Velocimetry (PDV). To measure the liner velocity during collapse, a twelve channel Mach-Zehnder PDV measurement system [16] is used. This consists of multiple 1 W fiber coupled 1550 nm lasers (IPG, LR-1-1550-SF) and 13 GHz photodetectors (Miteq, DR-125G-A). Data is recorded on oscilloscopes sampling at 1 GS/s.

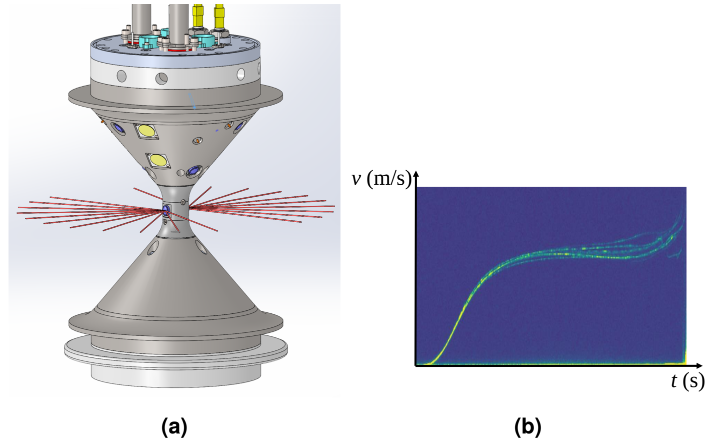

FIGURE 8: PDV diagnostic system in Prototype Zero: a) Model view of cones and PDV measurement chords, b) PDV spectrogram showing multiple overlaid velocity traces.

To achieve a high density of channels at the liner's equator a linear array of 12 single-mode fibers (Meisu Optics) is placed at the focal plane of a fisheye lens (ChanCCTV CH3741A) to create a fan of 12 PDV chords spread out over 180 degrees, as shown in Fig. 8a). This setup is mirrored to provide full azimuthal coverage. An alternate configuration swaps the fisheye lens for a ball lens to reduce optical power loss at the expense of less azimuthal coverage. The position of each measurement chord at two points is recorded and used to determine its vector in 3D space.

Raw PDV signals are transformed to velocity-time spectrograms as shown in Fig. 8b) that provide the velocity of the inner surface of the liner at various azimuthal positions. Velocity uncertainty of each chord is taken as the FWHM of the trace width, approximately ±4 m/s. The trace width is dependent on the laser linewidth and varies with the reflective properties of the lithium surface as its texture and shape change during implosion. PDV data is presented as the average over all the measurement chords with the uncertainty spanning the minimum and maximum values.

2.3.3 Direct Imaging. In the single-cone/window configuration, a high-speed camera captures an on-axis view of the cartridge *via* an overhead mirror (example frame is shown in Fig. 9). Camera calibration and extraction methods are identical to those previously reported in [12].

Briefly, a radial calibration grid is imaged on top of the window to allow for mirror and camera distortion correction. For all frames of the liner collapse, the inner and outer radii of the top liner surface are tracked and extracted as seen in Fig. 9. Correction of the extracted radii is done since the measurement plane is at a different height than the calibration plane. A radial measurement uncertainty of ±3 mm was determined based on positional uncertainties in the setup, calibration, height offsets, and extraction variability. The direct imaging radial data is presented as the average over the azimuthal coordinate with the uncertainty constituting the range of measurements.

TABLE 2: Shot parameters

		Liner Details				Shot Details			
Shot	Cartridge Configuration	Thickness (mm)	Outer Radius (mm)	Height (mm)	Mass (kg)	Liner Temperature (°C)	Circuits Active	Cap Voltage (kV)	Estimated Cap Energy (kJ)
A	None					N/A	4, 5, 6, 7	15.25	580.5
B	Two-cone	14.7	217.5	250	2.57	86	3, 4, 5, 6, 7	11.75	430.7
C	Single-cone/window	18.6	218.5	244	3.18	89	4, 5, 6, 7	15.25	580.5

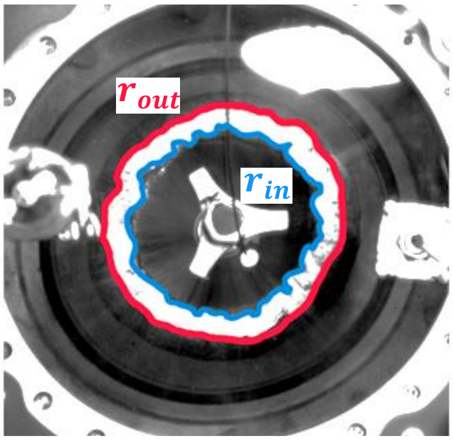

FIGURE 9: Direct imaging of liner in the single-cone/window configuration. Outer and inner extracted liner edges in red (r_{out}) and blue (r_{in}) respectively.

2.4 Shot Conditions

A total of 40 lithium cylinders were cast and compressed in the Prototype Zero experimental campaign. Additional tests were conducted in the absence of a cartridge and lithium cylinder to test components of the system in isolation, such as the power supply.

Three tests were chosen for the current study to validate the modelling methodology given the range of configurations. The operating conditions and dimensional information for these select shots are presented in Table 2.

Shot A is a test with no cartridge present, which was used to test the power supply. Shots B and C involved compression of a lithium cylinder, with operating conditions that best match what is expected in the full-scale machine. Shot B is a test in the two-cone configuration, enabling the use of PDV and SLR measurements for model validation. Shot C is in the single-cone/window configuration, allowing model validation through PDV and direct imaging measurements. The liner thicknesses for shots B and C were chosen such that the thickness-to-radius ratio falls within the operating range expected in the full-scale machine. The voltages used for each shot were selected to target the same kinetic energy per unit mass of the liner as in the full-scale machine.

3. NUMERICAL MODEL

ANSYS LS-DYNA (R16) was utilized to solve the coupled multi-physics dynamics of the lithium cylinder compressor. The simulation coupled the structural, thermal, and electromagnetic domains to capture the complex interactions.

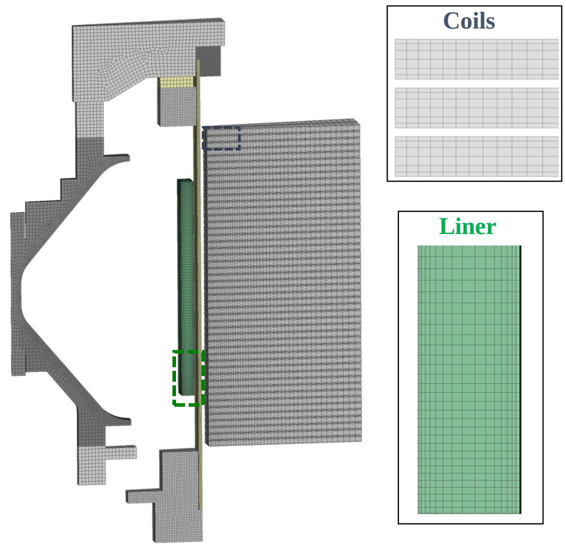

FIGURE 10: Mesh used in LS-DYNA for Shot B.

3.1 Model Setup

Simulations were conducted on a 3D geometry where the lithium cylinder, coil turns, and structural components were modeled as wedges with an angle span of $\theta = 2\pi/64$ and a thickness of two cells. Figure 10 illustrates the meshed geometry for the two-cone configuration. The setup represents an axisymmetric geometry where the electromagnetics are solved in 2D using the eddy current solver along the mid-plane of the domain. Structural and thermal dynamics are solved using 3D elements.

Adaptive time stepping was used for the EM solver, with a maximum time step of 2.5e-6 s and minimum of 1.0e-8 s. The FEM matrix was recomputed every time step. The BEM matrix was recomputed automatically based on the error calculation of the conductors' relative displacements, at intervals not exceeding 5 time-steps. Adaptive time stepping was also applied to the structural and thermal solvers, following the best practices outlined in Ref. [12].

The cartridge and coil geometries, along with some key dimensions, are shown in Fig. 11. The specifications of the cylinders are provided in Table 2. Each coil turn was simplified as a rectangular cross-section with dimensions of 177 mm x 6.4 mm (radial x axial). The axial spacing between each turn is 1.4 mm.

For both cartridge arrangements, a global maximum mesh size of 2 mm was used on the cross section. A structured mesh was generated for the conductive elements, which are highlighted in Fig. 11. To accurately capture the skin depth of the liner and coil turns, element size biasing was applied towards the outer

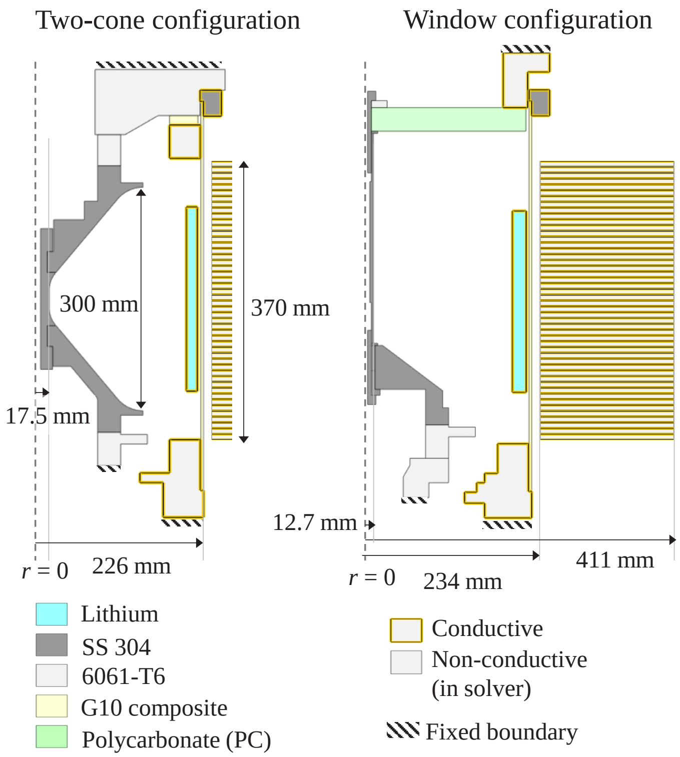

FIGURE 11: Initial geometry, materials, and boundary conditions used in LS-DYNA simulation for the two cartridge configurations. Conductive elements are indicated by a border drawn around them.

edges of the lithium cylinder, and the inner radius of the coil turns. Mesh settings for the liner and coil turns were based on guidelines outlined in [12].

The top and the bottom of the cartridge were fixed in all six degrees of freedom, as shown in Fig. 11. An out-of-plane constraint was applied to the faces normal to the azimuthal direction. Coils were constrained axially and allowed to expand radially. Structural bodies initially in contact were treated as bonded contacts, while the contact of the lithium with the structural components was prescribed a frictional contact with a coefficient of restitution of 0.5.

3.2 Material Models and Parameters

The materials used for the two cartridge configurations are shown in Fig. 12. The mechanical and thermal properties of solid lithium used in the simulations are provided in Table 3. A Johnson-Cook model (1) was used for lithium, which is commonly used to capture the flow stress dependence on strain hardening, strain-rate hardening, and thermal softening. The flow stress used in LS-DYNA is given by:

$$\sigma = \left[A + B\varepsilon_{\mathrm{p}}^{n}\right]\left[1 + C\ln\left(\frac{\dot{\varepsilon}}{\dot{\varepsilon}_0}\right)\right]\left[1 - T^{*m}\right] \tag{1}$$

where A, B, n, C, $\dot{\varepsilon}_0$, and m are material constants, ε_{p} is the equivalent plastic strain, $\dot{\varepsilon}$ is the strain rate, and T^* is the homologous temperature

$$T^* = (T - T_{\mathrm{ref}})/(T_{\mathrm{melt}} - T_{\mathrm{ref}}). \tag{2}$$

It is noted that the parameters presented in Table 3 differ from those presented in the previous study [15]. This discrepancy is due to re-fitting of the Johnson-Cook parameters using experimental data from a new load cell which offered more precise control over the strain rate and accounted for material thermal softening at elevated temperatures during testing.

TABLE 3: Material properties for lithium

Parameter	Value
Density, ρ (kg/m^3)	530
Elastic Modulus, E (GPa)	7.8
Poisson Ratio, ν	0.38
Initial Yield, A (MPa)	0.760
Hardening Constant, B (MPa)	1.38
Hardening Exponent, n	0.33
Reference Strain Rate, $\dot{\varepsilon}_0$	0.1
Strain Rate Constant, C	0.393
Thermal Softening Exponent, m	1.366
Melting Temperature, T_{melt} (°C)	180
Reference Temperature, T_{ref} (°C)	0
Thermal Conductivity, k (W m^{-1}°C^{-1})	84.8
Specific Heat, c_p (W m^{-1}°C^{-1})	3582

The remaining materials were assigned linear-elastic mechanical properties, as minimal plastic deformation is expected in the coils and structure. Additionally, deformation behavior falls outside the scope of this study.

Only specific components were modelled as electrically conductive, as highlighted in Fig. 12. Conductive components were defined with a relative magnetic permeability of unity using the keyword *EM_MAT_001 and assigned temperature dependent electrical conductivities. Components at the inner radius of the cartridge were treated as non-conductive since they are sufficiently far enough from the coils, resulting in a minimal impact from the magnetic field. This approach minimizes the computational time and avoids issues that arise when conductive elements come into contact.

3.3 Circuit Model

A simplified representation of the circuit and power supply discussed in Sec. 2.1 is included in the LS-DYNA model to supply the currents to the coils.

The *EM_CIRCUIT keyword is used to describe how the current density in each individual turn is modelled. Each turn must be modelled individually, and those connected in a coil are defined using the *EM_CIRCUIT_CONNECT keyword, which assures that the currents match within a single coil.

Multiple methods can be used to describe how the current is calculated in the *EM_CIRCUIT keyword, which is dependent on the value assigned to CIRCTYPE [17]. Two methods are used in the current study:

- CIRCTYPE = 1 : a time-dependent series for current is set from an input load curve. This is how test measurements for coil currents can be applied (as done previously in [12]) and to apply a current of zero for the open-circuited coils.
- CIRCTYPE = 30 : a newly developed circuit which represents turns connected to an RLC circuit with a diode (shown in Fig. 12).

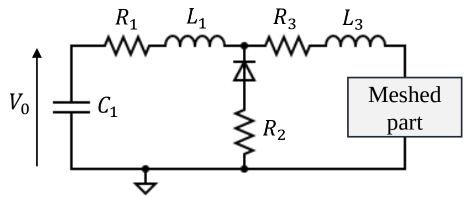

FIGURE 12: Schematic of circuit representing CIRCTYPE=30 in the *EM_CIRCUIT keyword in LS-DYNA.

TABLE 4: Relationship between circuit parameters used in simulation and those in the experimental apparatus.

Parameter in CIRCTYPE=30	Value from Prototype Zero parameters
V_0	$V_{\text{cap}}/N_{\text{turns}} * \sqrt{1 - X_{\text{loss}}}$
C_1	$C_{\text{cap}} * N_{\text{turns}}/2$
R_1	$R_{\text{cap}}/N_{\text{turns}}$
L_1	$\left(L_{\text{cap}} - L_{\text{diode}}\right)/N_{\text{turns}}$
R_2	$R_{\text{diode}}/N_{\text{turns}}$
R_3	$R_{\text{cable}}/N_{\text{turns}}$
L_3	$\left(L_{\text{switch}} + L_{\text{diode}}\right)/N_{\text{turns}}$

The parameters used in CIRCTYPE = 30 to represent each turn of the circuit and their relationship to the experimental circuit are listed in Table 4.

The system's energy input is derived from the total capacitor energy, given by

$$E_{\text{cap}} = \frac{1}{2}CV^2. \tag{3}$$

Previous studies have shown that the 2D axisymmetric formulation may predict a more efficient energy transfer from the capacitors to the liner than observed in experiments [12]. This discrepancy can arise from factors such as three-dimensional effects, additional resistive losses, or uncertainties in circuit and material properties.

To account for these additional losses, which are not captured in the simulation, a linear loss factor, X_{loss}, is introduced. The effective energy input is then adjusted as

$$E_{\text{in}} = E_{\text{cap}}(1 - X_{\text{loss}}). \tag{4}$$

This loss factor is included in the input voltage, as shown in Table 4, and ranges from 0% and 20% in simulation.

4. RESULTS

The simulation methodology is validated using the three test shots presented in Table 2.

4.1 Circuit Validation (Shot A)

Figure 13 shows the evolution of coil currents for Shot A, comparing simulation without voltage scaling (dashed) to measurements from test (solid) for the activated coils. Transparent bands on test data represent an estimated measurement uncertainty of ±5%.

Current traces from experiment and simulation show peak currents up to 70 kA and rise times of approximately 0.2 ms. In the simulation, the pair coils have equal currents. However, experimental measurements show asymmetry, particularly between

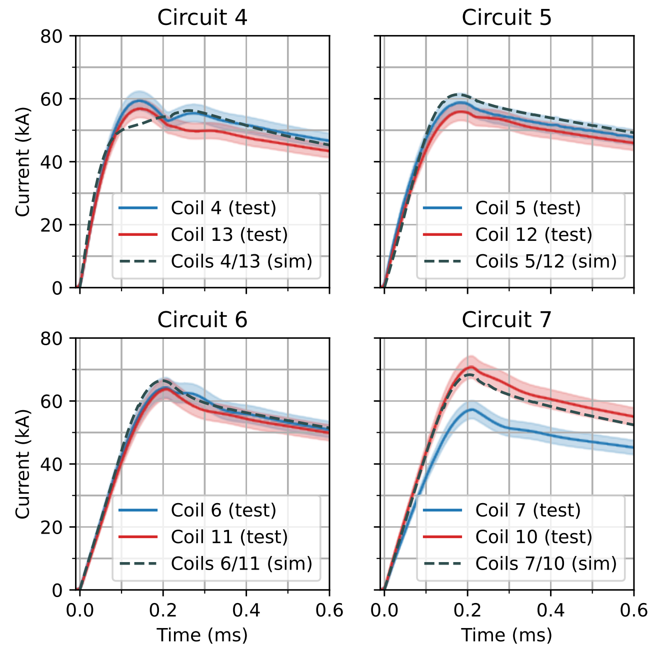

FIGURE 13: Evolution of coil currents measured in the experiment and compared with simulation for Shot A with no additional losses included.

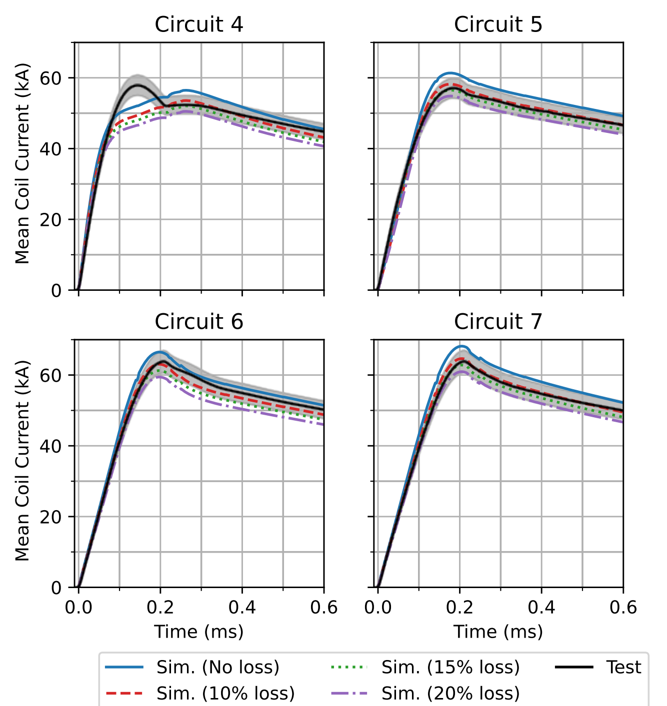

FIGURE 14: Average currents from activated pair coils, measured from test and compared with simulation for different energy loss factors.

coils 7 and 10, where the peak current in coil 7 is 56 kA, which is 20% lower than the 70 kA observed in coil 10.

Simulations considering additional energy losses of 10%, 15%, and 20% were completed. The average current through each coil pair was computed to compensate for asymmetries in the coil currents seen in experiment. Figure 14 shows the average currents for each circuit from experiment and each scaled simulation.

TABLE 5: Relative error in magnetic energy estimate between simulation and test.

X_{loss} / Circuit	$\left(\left(\int I^2 dt\right)_{\text{sim}} - \left(\int I^2 dt\right)_{\text{test}}\right) / \left(\int I^2 dt\right)_{\text{test}}$ 0%	10%	15%	20%
Circuit 4	0.055	-0.050	-0.104	-0.156
Circuit 5	0.146	0.031	-0.027	-0.084
Circuit 6	0.085	-0.024	-0.078	-0.132
Circuit 7	0.151	0.035	-0.022	-0.080
Average	**0.109**	**0.002**	**-0.060**	**-0.101**

The average current squared, which is proportional to the magnetic energy in the coils, is integrated up to 0.6 ms to quantify the differences between test and simulations. The relative differences between test and simulations with different loss factors are shown Table 5. Results aligned closest between test and simulation when including an additional 10% energy loss.

4.2 Liner Trajectory

Shots B and C from Table 2 were simulated to compare the liner trajectories with simulation.

4.2.1 Two-Cone Configuration (Shot B). Figure 15 shows an evolution of the liner predicted by simulation for Shot B with a 10% loss factor. Conductive elements are coloured by the magnitude of the magnetic field in the components. The liner impacts the cones at approximately 0.45 ms and impacts the center of the cone shortly after the final frame of 0.6 ms.

Figure 16 shows a comparison of the inner surface of the liner from the simulation with SLR from test at different time instances, for the case shown in Fig. 15. The final measurement from SLR is at 0.47 ms. The transparent band represents measurement uncertainty for the liner's front edge.

Figure 17 shows the evolution of the radial velocity at the equator extracted from simulations and compared with measurements taken by PDV in the test. Experimental measurements show the liner accelerates up to -300 m/s before signal is lost at 0.52 ms. Simulation predictions with a 10% loss factor lie within the deviations and uncertainty bands from test, with the simulation yielding a similar radial velocity up to 0.5 ms.

4.2.2 Window Configuration (Shot C). Figure 18 shows snapshots of the liner trajectory simulated for Shot C with a loss factor of 20%.

Figure 19 shows the evolution of the radial velocity at the equator extracted from simulations and compared with measurements taken by PDV in Shot C. Experimental measurements show the liner accelerate up to approximately -320 m/s before it begins accelerating even further after 0.6 ms, with a peak measured velocity of -500 m/s before signal is lost. Simulation predictions with an energy loss factor of 20% most accurately match test, lying within the deviations and uncertainty bands from test.

Figure 20 shows the positions of the liner's edges (top inner, top outer, and equator) extracted from this simulation and compared against measurements from experiment *via* PDV and direct imaging. The coloured translucent bands represent the measurement uncertainty and the variation between the maximum and minimum measurements for the specific edge.

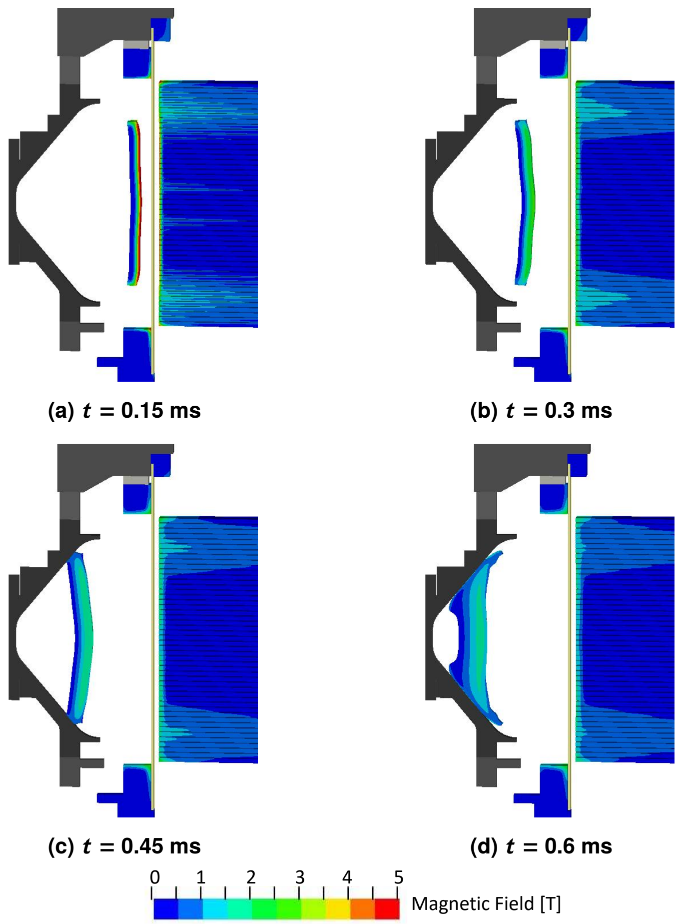

FIGURE 15: Evolution of liner shape and magnetic field intensity (in EM components) for Shot B with 10% additional energy loss.

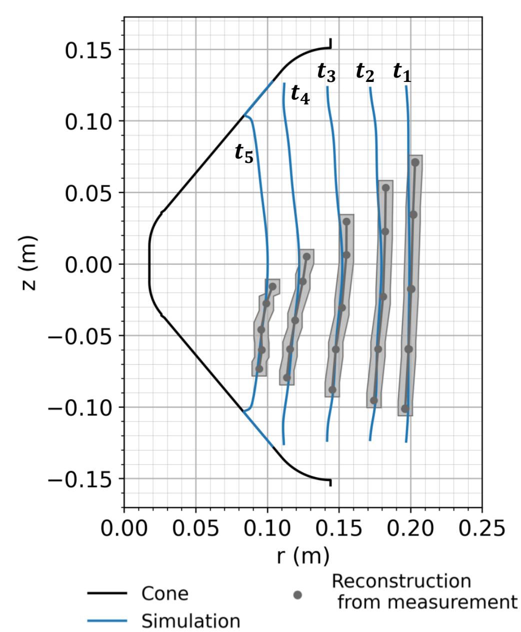

FIGURE 16: Comparison of the inner surface of the liner from simulation (with a 10% loss factor) and SLR measurements for Shot B. Transparent sections represent measurement uncertainty. Data shown for time instances t (in ms) = [0.1, 0.2, 0.3, 0.4, and 0.47].

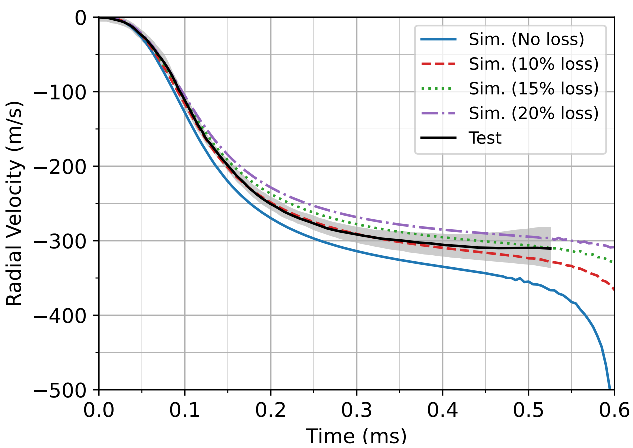

FIGURE 17: Evolution of the radial velocity at the inner equator for Shot B – comparing test and simulations with different levels of energy losses.

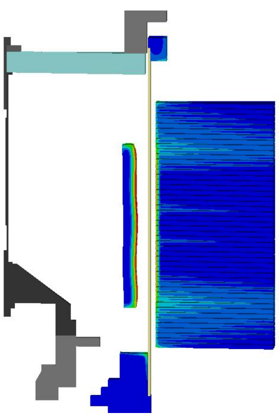

(a) t = 0.15 ms

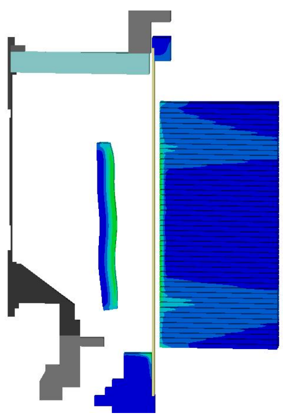

(b) t = 0.3 ms

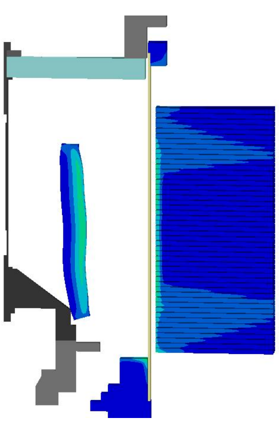

(c) t = 0.45 ms

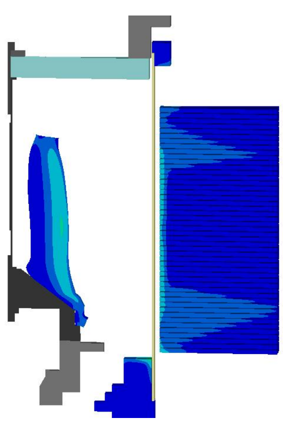

(d) t = 0.6 ms

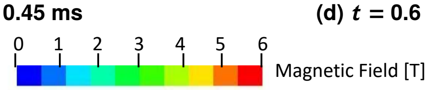

FIGURE 18: Evolution of liner shape and magnetic field intensity (in EM components) for Shot C with 20% additional losses.

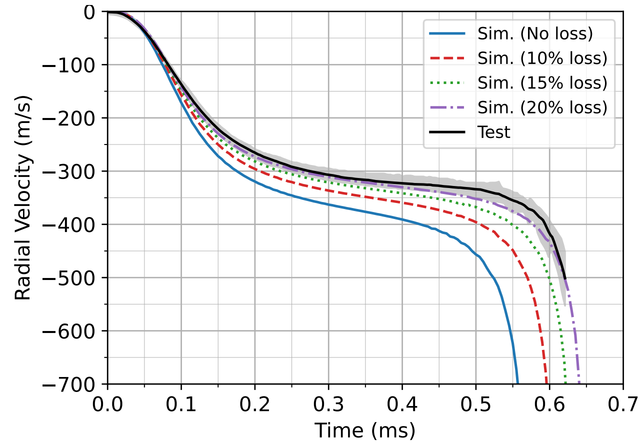

FIGURE 19: Evolution of the radial velocity at the inner equator for Shot C – comparing test and simulations with different levels of energy losses.

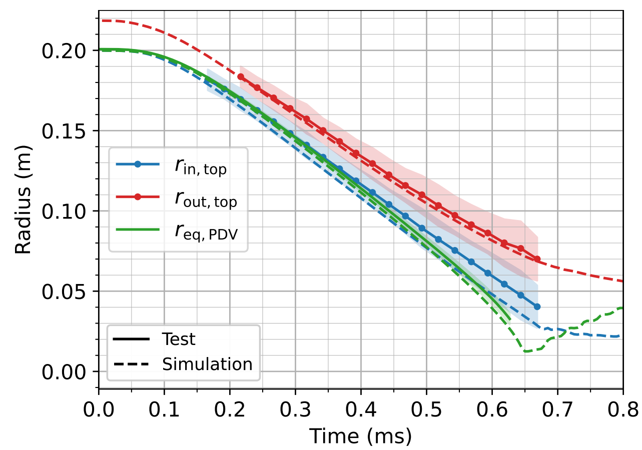

FIGURE 20: Comparison between test and simulation for the evolution of outer (top) and inner (top and equator) cylinder radii over time for Shot B with a 20% energy loss factor. Transparent bands represent the uncertainty and range in radius measured along each circumference.

5. DISCUSSION

The objective of this study is to evaluate the use of simulation to predict the shape and trajectory of a solid lithium liner undergoing electromagnetic compression. This is accomplished by evaluating the capability of the LS-DYNA circuit model to predict the coil current, and by comparing the resulting liner trajectory with diagnostic measurements.

5.1 Circuit Model

Circuit model validation is achieved using measurements from Shot A. This configuration involved connecting half of the coils to the power supply (circuits 4, 5, 6 and 7), and discharging into an empty cavity (no cartridge).

Figure 13 shows that the circuit model can replicate similar current profiles to the ones measured in Shot A. However, the model slightly overpredicts the amplitude of the coil currents in most of the circuits. Table 5 shows that in the absence of additional losses included in the model, the simulation computed approximately 10% more magnetic energy than the experiment. While an alignment within 10% is a significant achievement in the model validation, further analyses were completed in this study to achieve closer agreement with experimental data.

The higher efficiency calculated in the model can potentially be explained by parasitic inductance losses, contact resistances between the cables, coil azimuthal asymmetries, or electrical specification variations across the pulse power components. These effects are particularly noticeable when comparing the measured coil currents connected in the same circuit. For instance, circuit 7 showed a difference of close to 15 kA of peak amplitude between the two coils. Modeling each source of resistive and inductive losses in the circuit model would require intensive calibration. Therefore, it was proposed to include these additional losses by modifying the total initial electrical energy.

Results shown in Fig. 14 and Table 5 compared the circuit currents between the test and simulations with the input electrical energy reduced by 0%, 10%, 15%, and 20%. The results assuming additional losses of 10% and 15% aligned the closest with the experimental measurements, indicating that up to 15% of the initial electrical energy is lost across mechanisms not captured in the current model. This is reasonably acceptable for the 2D axisymmetric model using a simplified RLC circuit with limited resistance and inductance calibration.

From this validation exercise, it was noted that connecting coil pairs in series as opposed to in parallel is preferable to avoid undesired magnetic pressure gradients caused by different coil currents during compression. More tests should be performed on the LM26 compressor to better understand energy loss mechanisms.

5.2 Liner Trajectory

Shots B and C are used to assess the capability of the LS-DYNA simulation methodology to predict the compression trajectory of a cylindrical lithium liner.

In Shot B, the liner velocity was tracked at the equator by PDV (Fig. 17) and its axial profile was reconstructed by the SLR measurements (Fig. 16). Following the conclusions from Shot A, a simulation with additional losses of 10% was used, which resulted in a liner trajectory that aligns closely with SLR reconstruction. The liner velocity at the equator closely aligns with available PDV measurements, within the range of velocities measured by the channels.

The simulation's ability to replicate the axial profile and the liner velocity up to 0.47 ms is an important achievement. This capability is required for LM26, where the reconstruction of the plasma compression sequence will require close alignment between the simulation and the experimental liner trajectory.

Shot C used a single-cone/window configuration. The liner velocity was tracked at the equator by PDV (Fig. 19) while direct imaging tracked the position of the top edges of the liner (Fig. 20). The best alignment between simulation and experimental data was with an additional energy loss of 20% included in the model. Figure 19 shows that simulation accurately predicts the liner velocity at the equator, including the rapid acceleration at the end of compression due to the geometrical convergence of the liner. This effect was also simulated for Shot B, but the PDV signal was lost before it could be detected in test.

The different estimate on losses between Shot B and Shot C may be explained by the differences in cartridges and operating conditions. Shot B used five circuits during compression, while Shot C used four. Variations in mutual coupling between the activated coils, open-circuited coils, the liner, and the cartridge components could have led to different levels of additional losses in each shot.

Another source of energy loss differences between Shot B and Shot C may be attributed to the liner geometry. The liner used in Shot C is thicker than that used in Shot B (18.6 mm *vs*. 14.7 mm). As the liner thickness increases the hoop stress resisting deformation also increases. As a result, the trajectories are particularly sensitive to the material model parameters used to describe the flow stress in lithium (Table 3). The parameters used in this study were obtained from fitting the Johnson-Cook model (Eq. (1)) to test data obtained in-house. The propagation of the model residual error to the trajectory predictions has not been evaluated but could significantly affect the velocity of the liner, especially at high strain and high strain-rates. Therefore, simulation prediction might deviate from measurements deep in compression and for thicker liners.

6. CONCLUSION

Electromagnetic compression of hollow lithium cylinders was achieved using theta-pinch coils on General Fusion's Prototype Zero testbed. A 2D axisymmetric model was developed in LS-DYNA and validated against experimental results. The modelling approach integrated the electromagnetic solver with a newly developed circuit model, improving its predictive capabilities compared to previous simulation work [12].

Three test shots (A, B, C) were selected for the validation of the numerical model. Shot A did not include a liner and was used to validate the circuit model. Shots B and C included a liner and were used to validate the capability of LS-DYNA to capture the liner's dynamics during compression. For all test shots, the model estimated greater efficiency in transferring energy to the coils and liner than indicated by experimental measurements. When additional energy losses ranging from 10% to 20% were included, the simulations achieved close alignment with experimental data. These loss estimates are realistic given the modelling and experimental uncertainties. Since only three test shots were compared between simulation and test, further comparisons are required to improve confidence in the modelling tools and investigate energy loss mechanisms. However, the alignment between the simulation results and test data indicates a promising first step in model validation.

The improved simulation methodology presented in this study, which includes a method to account for additional system losses, demonstrates reliable predictive capabilities to inform operation of similar machines. These advancements guided the design of the full-scale LM26 plasma compression machine and enabled the reconstruction of liner trajectories necessary for computing plasma compression performance.

ACKNOWLEDGMENTS

The authors are thankful for the continuous support by ANSYS-LST (Pierre L'Eplattenier and Iñaki Çaldichoury) and Simutech Group. The authors also wish to thank the entire General Fusion team for making this work possible.

REFERENCES

[1] Laberge, M. "Magnetized target fusion with a spherical tokamak." *Journal of Fusion Energy* Vol. 38 No. 1 (2019): pp. 199–203.

[2] Es' kov, AG, Zolotovsky, OA, Kurtmullaev, R Kh, Lauhin, Ya N, Malyutin, AJ, Markin, AJ and Semenov, VN. "Experiments on producing the plasma of high-β by longitudinal shock waves." *European Conference on Controlled Fusion and Plasma Physics*. 1973.

[3] Turchi, PJ, Cooper, AL, Ford, RD, Jenkins, DJ and Burton, RL. "Review of the NRL liner implosion program." *Megagauss Physics and Technology* (1980): pp. 375–386.

[4] Moses, RW, Krakowski, RA and Miller, RL. "Conceptual design of the Fast-Liner Reactor (FLR) for fusion power." Technical Report No. LA-7686-MS. Los Alamos National Lab.(LANL), Los Alamos, NM (United States). 1979.

[5] Howard, SJ, Reynolds, M, Froese, A, Zindler, R, Hildebrand, M, Mossman, A, Donaldson, M, Tyler, T, Froese, D, Eyrich, C et al. "Measurement of spherical tokamak plasma compression in a PCS-16 magnetized target fusion experiment." *Nuclear Fusion* Vol. 65 No. 1 (2024): p. 016029.

[6] Froese, A, Zindler, R, Herunter, M, Macdonald, C, Chisholm, T, Krotez, D, Hildebrand, M, Tancetti, A, Kelly, B, Love, E, Mossman, A and Reynolds, M. "Bayesian Equilibrium Reconstruction for General Fusion Demonstration Plant [poster]." *64th Annual Meeting of the APS Division of Plasma Physics, Spokane, Washington, October 17-21, 2022*.

[7] Froese, A, Reynolds, M, Suponitsky, V, Dick, J-S, Segas, R, Hung, CP, Khalzov, I, Sirmas, N, Ross, D, Roberts, D and Brennan, D. "Expected MHD Stability and Error Field Penetration in LM26 Magnetized Target Fusion Experiment at General Fusion [Poster]." *66th Annual Meeting of the APS Division of Plasma Physics, Atlanta, Georgia, October 7-11, 2024*.

[8] Mangione, NS, Wu, H, Preston, C, Lee, AMD, Entezami, S, Ségas, R, Forysinski, PW and Suponitsky, V. "Shape manipulation of a rotating liquid liner imploded by arrays of pneumatic pistons: Experimental and numerical study." *Fusion Engineering and Design* Vol. 198 (2024): p. 114087.

[9] Epp, K, Rablah, R, Howard, S, Laberge, M, Reynolds, M, Ivanov, R, Carle, P, Young, W, Froese, A, Gutjahr, C et al. "Confinement Physics on Plasma Injector 3." *APS Division of Plasma Physics Meeting Abstracts*, Vol. 2020: pp. ZP07–011. 2020.

[10] Carle, P, Howard, S, Tancetti, A, Antony, A, Ribeiro, C, Coop, S, Braglia, F, Rohollahi, A, Feng, X, Radich, A et al. "Physics Conclusions of PI3 Spherical Tokamak Program [Poster]." *66th Annual Meeting of the APS Division of Plasma Physics, Atlanta, Georgia, October 7-11, 2024*.

[11] Tancetti, A, Ribeiro, C, Howard, S, Coop, S, McNally, C, Reynolds, M, Kholodov, P, Braglia, F, Zindler, R, MacDonald, C et al. "Thermal energy confinement time of Spherical Tokamak plasmas in PI3." *Nuclear Fusion* Vol. 65 No. 3 (2025).

[12] Dick, J-S, Sirmas, N, Bernard, S, Santos, L and Forysinski, P. "Electromagnetic Lithium Ring Compression for Magnetized Target Fusion Application: Trajectories." *Proceedings of ASME 2024 Pressure Vessels & Piping Conference, July 28–August 2, 2024, Bellevue, Washington, USA*. DOI 10.1115/PVP2024-121781.

[13] Edalatfar, F, Santos, L, Jayhooni, H and Dick, J-S. "Electromagnetic Lithium Ring Compression for Magnetized Target Fusion Application: Shell Buckling." *Proceedings of ASME 2024 Pressure Vessels & Piping Conference, July 28–August 2, 2024, Bellevue, Washington, USA*. DOI 10.1115/PVP2024-123079.

[14] LSTC. *EM THEORY MANUAL - Electromagnetism and Linear Algebra in LS-DYNA* (2012).

[15] Miao, Y, Sexsmith, M, Hartono, S, Preston, C, Tsai, B, Dick, J-S and Sirmas, N. "Strain-Rate-Dependent Parameters of Lithium as a Plasma Facing Material for Magnetized Target Fusion Application." *Proceedings of ASME 2024 Pressure Vessels & Piping Conference, July 28–August 2, 2024, Bellevue, Washington, USA*. DOI 10.1115/PVP2024-123063.

[16] Dolan, D. H. "Extreme measurements with Photonic Doppler Velocimetry (PDV)." *Review of Scientific Instruments* Vol. 91 No. 5 (2020): p. 051501.

[17] LSTC. *LS_DYNA R16 Keyword Manual Vol III* (2025).